Enabling High Accuracy Distance Measurements With FMCW Radar Sensors

Lukas Piotrowsky, *Student Member, IEEE*, Timo Jaeschke, *Member, IEEE*, Simon Kueppers, *Student Member, IEEE*, Jan Siska, *Student Member, IEEE*, and Nils Pohl, *Senior Member, IEEE*

***Abstract*— With the integrated radar technology being increasingly common in the automotive segment, it becomes even more cost-effective in other applications as well. Taking into account its price and robustness, radar sensors can be considered as a potential replacement for laser interferometry which is being widely used for accurate contactless sensing. In this paper we describe a phase evaluation algorithm for highly accurate distance measurements using linear frequency modulated continuous wave (FMCW) radar systems, considering hardware dependent effects i. e. frequency responses of the signal paths. In several investigations we show that this novel algorithm is significantly more robust against disturbing radar targets or micro vibrations than typical techniques. Distance measurements were carried out using an 80 GHz wideband FMCW radar sensor on a maximum measurement range of 5.2 m with a movable radar target. For free space measurements the unambiguous measurement accuracy was improved to ±4.5 µm, using phase evaluation techniques in a non-ideal environment over the entire measurement range, which was previously around ±120 µm with frequency evaluation techniques. Due to its robustness and accuracy, the proposed algorithm is well suited for harsh industrial environments such as real time positioning of machine tools.**

***Index Terms*— Distance measurement, estimation error, millimeter wave radar, radar measurements, radar theory, signal processing algorithms, ultra wideband radar.**

I. Introduction

THESE days there are huge varieties of methods for contactless micro- and macroscopic distance measurements. In particular, industrial positioning used in machine tools typically requires accuracies to the extent of a few micrometers. Thus accurate, robust and cost-effective methods for distance measurements suitable for machine controlling are required.

Manuscript received May 2, 2019; revised June 28, 2019; accepted July 9, 2019. Date of publication September 18, 2019; date of current version December 27, 2019. This work was supported in part by the European Union and the Federal State North Rhine-Westphalia in frame of the European Regional Development Fund (ERDF) and in part by the German Research Foundation (DFG) through the Project SFB/TRR 196 "MARIE" under Project M04. This article is an expanded version from the IEEE MTT-S International Microwave Symposium (IMS 2019), Boston, MA, USA, June 2–7, 2019. *(Corresponding author: Lukas Piotrowsky.)*

L. Piotrowsky, J. Siska, and N. Pohl are with the Insitute of Integrated Systems, Ruhr University Bochum, 44801 Bochum, Germany (e-mail: lukas.piotrowsky@rub.de).

T. Jaeschke and S. Kueppers are with 2π-Labs GmbH, 44801 Bochum, Germany.

Color versions of one or more of the figures in this article are available online at http://ieeexplore.ieee.org.

Digital Object Identifier 10.1109/TMTT.2019.2930504

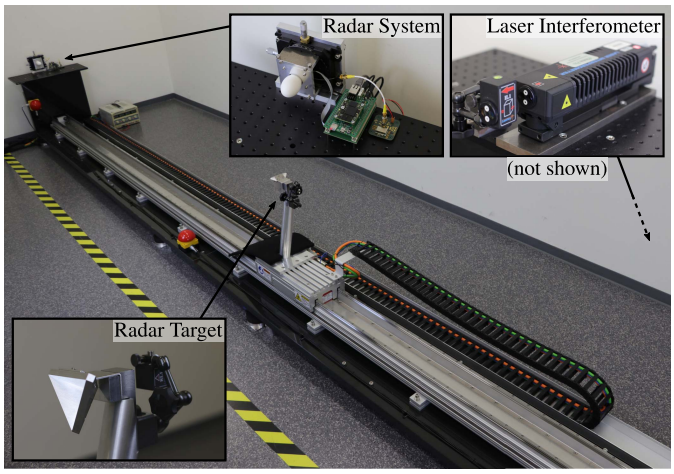

Fig. 1. Photograph of the setup used for experimental evaluation. Consisting of a laser interferometer referenced 80 GHz FMCW radar sensor and a corner reflector used as a radar target placed on a linear track with 5.2 m working range.

For accurate distance measurements, laser interferometry is the most commonly used technology. However, especially in harsh environments dust, steam and flying chips can result in a loss of measurability when using optical sensors. Frequency modulated continuous wave (FMCW) radar on the other hand can be used as a robust and cost-effective alternative as shown in this work. Their working principle allows measuring multiple unambiguous distances simultaneously and also, they can automatically recover from short term interferences unlike laser interferometers. As can be seen, there is a demand for advanced FMCW radar signal processing, that enables this high measurement accuracy.

In our previous work [1] we outlined a novel algorithm that uses a combination of the downconverted intermediate frequency (IF) signal phase with its frequency, taking into account the information of the parasitic hardware. In this work we give a more theoretical and in-depth view considering disturbing radar targets and micro-Doppler dependent effects. Furthermore, simulations and measurements with an optimized experimental setup as well as radar hardware were performed. As a result, we have achieved significantly better measurement performance than in [1]. Fig. 1 shows a photograph of the experimental setup used for experimental evaluation. As a testing platform, a wideband FMCW radar with a center

TABLE I
OVERVIEW OF THE PUBLISHED HIGH ACCURACY RADAR MEASUREMENTS

Technology	Frequency / Bandwidth (GHz)	Accuracy (μm)	Range (m)	Year / Reference
FMCW/CW Radar	10.5 / 2	±1000	0.35	1993 / [24]
FMCW Radar	24 / 3	±800	17	2003 / [11]
Network Analyzer	26 / 4	±1000	4	2006 / [12]
FMCW Radar	24 / 8	±250	2.75	2012 / [13]
FMCW Radar	80 / 25.6	±350	3	2012 / [14]
FMCW Radar	80 / 25.6	±4	0.05	2013 / [15]
FMCW Radar	122 / 0.792	±20 000	6	2013 / [16]
Six-Port Radar	24 / -	±200	0.07	2013 / [17]
Six-Port Radar	24 / -	±250	0.15	2014 / [18]
FMCW Radar	146 / 48	±1	0.01	2014 / [19]
FMCW Radar	61 / 0.5	±26	0.03	2014 / [20]
FMCW Radar	24 / 1	±5	0.05	2015 / [8]
FMCW Radar	122 / 1	±200	1.9	2015 / [21]
FMCW Radar	80 / 25	±15	0.08	2017 / [22]
FMCW Radar	124 / 6	±6	0.035	2017 / [9]
FMCW Radar	80 / 20	±8	3.8	2019 / [1] [a]
FMCW Radar	**80 / 24**	**±4.5**	**5.2**	**2019 / -** [b]

[a] Previous work
[b] This work

operating frequency of 80 GHz (see [2], [3]) was utilized. The chosen radar hardware still sets standards in terms of relative bandwidth and phase noise level.

In various applications [4]–[10] it has previously been shown how to perform unambiguous IF phase evaluation with FMCW radar systems. However, compared with the phase evaluating algorithm proposed here, unwanted hardware specific effects were not considered. Furthermore, the phase evaluating methods [8], [9] are more computationally intensive due to their iterative behavior. Table I shows an overview of the published free space radar high accuracy measurements with at least 10 mm measurement range. In [8], [9], [11]–[22] it was shown that highly accurate measurements using radar technology are basically possible. However, the investigated measurement range in these publications were significantly below one meter. This was extended up to 5.2 m in this work, to better suit the needs of industrial applications. Unlike the FMCW radar technology, the six-port interferometry used in [17], [18] does not allow simultaneous measurements of multiple radar targets. In addition, it is not able to measure unambiguous distances in general. The distance measurement precision with FMCW radar systems, which is not primarily considered here, was previously analyzed in [23], where they presented an analytical way to describe noise in phase-locked loop stabilized FMCW radar systems in a theoretic manner.

At first, in Section II-A we show some partially new methods for accurate distance measurements using intermediate frequency evaluation (FE) and discuss their performance by simulation. FE is an integral part of the phase evaluation (PE) algorithm, originally published in [1], which is discussed in detail in Section III. Therefore, FE should be considered properly. The PE algorithm is divided into so called basic PE and enhanced PE which is based on basic PE. Then, in Section IV we compare FE with PE theoretically from different perspectives. Finally, in Section V we confirm the theory by simulations and measurements.

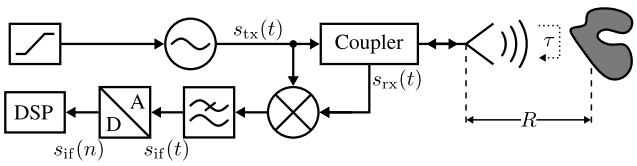

Fig. 2. Simplified block diagram of a monostatic FMCW radar system.

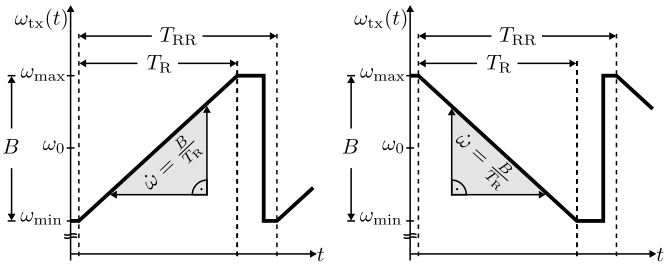

Fig. 3. Sawtooth shaped frequency modulation of an FMCW radar system with either up- or downchirps. T_{RR} is the ramp repetition time. The frequency chirp runs between $\omega_{\min}$ and $\omega_{\max}$.

II. DISTANCE ESTIMATION USING FMCW RADAR

Fig. 2 shows the simplified block diagram of the investigated monostatic FMCW radar. A carrier signal with the center angular frequency ω_0 is frequency modulated by a linear frequency chirp as shown in Fig. 3:

$$s_{\mathrm{tx}}(t) = A_{\mathrm{tx}} \cdot \cos\left(\omega_0 t + \int \pm\dot{\omega} t \,\mathrm{d}t\right), \quad -\frac{T_{\mathrm{R}}}{2} \le t \le \frac{T_{\mathrm{R}}}{2}$$
$$= A_{\mathrm{tx}} \cdot \cos\left(\omega_0 t \pm \frac{1}{2}\dot{\omega} t^2 + \phi_{\mathrm{m}}\right), \tag{1}$$

where A_{tx} is the amplitude of the transmitted signal $s_{\mathrm{tx}}(t)$, $\dot{\omega}$ is the quotient of the ramp bandwidth B, T_{R} is the ramp duration and ϕ_{m} is the zero-phase term of the phase modulation. A plus/minus sign $\pm$ or $\mp$ in all equations apply to rising and falling frequency ramps, respectively. The signal $s_{\mathrm{tx}}(t)$ is then radiated via an antenna into free space and reflected by a radar target. After a round-trip propagation delay τ the signal

$$s_{\mathrm{rx}}(t) = A_{\mathrm{rx}} \cdot \cos\left[\omega_0(t-\tau) \pm \frac{1}{2}\dot{\omega}(t-\tau)^2 + \phi_{\mathrm{m}} + \phi_{\mathrm{r}}\right], \tag{2}$$

is received by the same antenna, where A_{rx} is the amplitude of the received signal and ϕ_{r} is the target reflection phase component which mainly depends on the properties of the target. After reception, $s_{\mathrm{rx}}(t)$ is downconverted to the IF signal. The resulting idealized IF signal of the linear frequency modulated FMCW radar is

$$s_{\mathrm{if}}(t) = A_{\mathrm{if}} \cdot \cos\left(\dot{\omega}\tau t \pm \omega_0 \tau - \frac{1}{2}\dot{\omega}\tau^2 \mp \phi_{\mathrm{r}}\right), \tag{3}$$

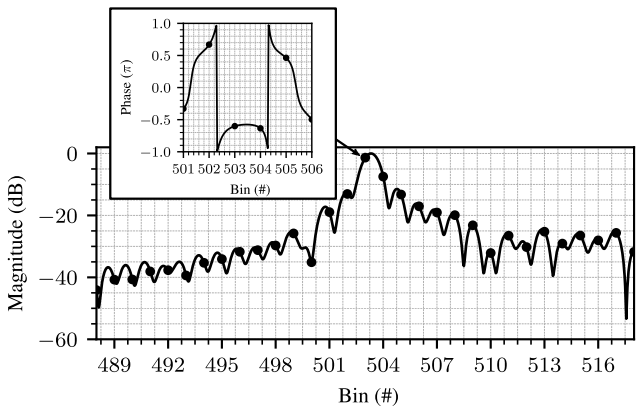

Fig. 4. Example for a magnitude and the corresponding phase spectrum of the discrete Fourier transformed IF signal. The continuous lines were produced by zero-padding.

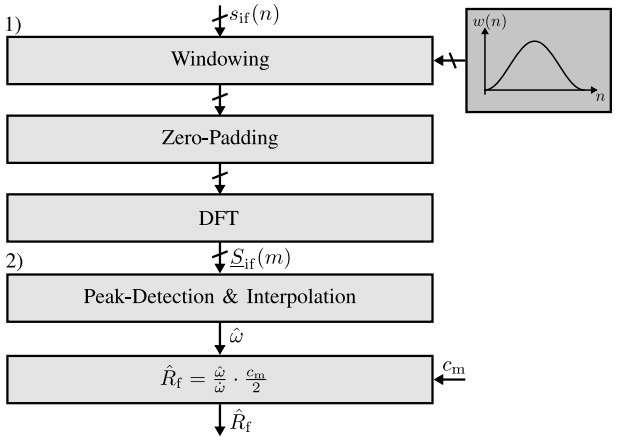

Fig. 5. Flow diagram for distance estimation by frequency evaluation using interpolation.

where A_{if} is the amplitude of the IF signal. The distance from the radar system to the radar target is then calculated from the frequency or phase information of the IF signal using τ.

A. Extension of the Classical Frequency Based Approach

Typically, the distance is determined by estimating the intermediate frequency ω_{if}. Distance R is then calculated from the relationship $\tau = 2R/c_{\mathrm{m}}$ as

$$R = \frac{\omega_{\mathrm{if}}}{\dot{\omega}} \cdot \frac{c_{\mathrm{m}}}{2}, \tag{4}$$

where c_{m} is the propagation speed of electromagnetic waves in the specific medium. Estimation of the intermediate frequency is mostly performed by simple spectral analysis as shown in Fig. 4. The magnitude spectrum of the discrete Fourier transformed (DFT) intermediate frequency $\underline{S}_{\mathrm{if}}(m)$ serves as the maximum likelihood function for the estimator. Consequently, the maximum-likelihood estimated frequency bin is

$$\hat{m} = \arg\max_{m} |\underline{S}_{\mathrm{if}}(m)| = \frac{\dot{\omega}\tau N}{\omega_{\mathrm{s}}}, \tag{5}$$

where N is the number of data samples and ω_{s} is the sampling angular frequency used. As a result the estimated distance for the FE is

$$\hat{R}_{\mathrm{f}} = \frac{2\pi\hat{m}}{B} \cdot \frac{c_{\mathrm{m}}}{2}. \tag{6}$$

Due to the discretely estimated frequency bin, the range resolution of this comparatively coarse FE is

$$\Delta\hat{R}_{\mathrm{f}} = \frac{2\pi}{B} \cdot \frac{c_{\mathrm{m}}}{2}. \tag{7}$$

Interpolation or zero-padding is required to obtain a higher frequency and thus range accuracy. In the following, different methods of interpolation in the IF magnitude spectrum are examined. Sampling a harmonic in a finite time interval results in a spectral convolution with a sinc pulse if the sampling time is not an integer multiple of the harmonics period duration. This phenomenon is commonly called spectral leakage. Spectral leakage can be reduced by multiplication of $s_{\mathrm{if}}(t)$ with a window function unlike a rectangular window prior to the DFT. Thus, the window function shapes the spectral pulse and should be considered by the spectral interpolation to reduce an unwanted frequency dependent bias. The most common way of magnitude spectrum interpolation is a three-point parabolic interpolation

$$\hat{m}_{\mathrm{i,pi}} = \hat{m} - \frac{|\underline{S}_{\mathrm{if}}(\hat{m})| - |\underline{S}_{\mathrm{if}}(\hat{m}+1)|}{2|\underline{S}_{\mathrm{if}}(\hat{m})| - |\underline{S}_{\mathrm{if}}(\hat{m}+1)| - |\underline{S}_{\mathrm{if}}(\hat{m}-1)|} + \frac{1}{2}, \tag{8}$$

whereby the two frequency bins adjacent to the maximum estimated in (5) are used to fit a parabola inside the magnitude spectrum. A different type of three-point interpolation is initially proposed in [25] as exponential parabolic interpolation

$$\hat{m}_{\mathrm{i,epi}} = \hat{m} - \frac{|\underline{S}_{\mathrm{if}}(\hat{m})|^p - |\underline{S}_{\mathrm{if}}(\hat{m}+1)|^p}{2|\underline{S}_{\mathrm{if}}(\hat{m})|^p - |\underline{S}_{\mathrm{if}}(\hat{m}+1)|^p - |\underline{S}_{\mathrm{if}}(\hat{m}-1)|^p} + \frac{1}{2}. \tag{9}$$

Using the exponential parabolic interpolation, a non-integer exponent p is introduced. The influence on FE bias related to spectral leakage can be significantly reduced with an optimized value for p, which depends only on the window function used.[1] A further kind of interpolation is the center formula

$$\hat{m}_{\mathrm{i,cf}} = \frac{\sum_{m=\hat{m}-m_{\mathrm{n}}}^{\hat{m}+m_{\mathrm{n}}} m \cdot |\underline{S}_{\mathrm{if}}(m)|^2}{\sum_{m=\hat{m}-m_{\mathrm{n}}}^{\hat{m}+m_{\mathrm{n}}} |\underline{S}_{\mathrm{if}}(m)|^2}, \tag{10}$$

which is frequently used in spectral analysis referred as the spectral centroid with frequency band limitation. This approach is based on the formula for the center of mass from discretely distributed masses using the power spectral density. m_{n} belongs to the one-sided number of bins beneath the discrete maximum used for center calculation. Simulations have shown that a minimum value of five is needed independent of the used window function. A further increase of m_{n} does not lead to a significant reduction of the bias. Furthermore, m_{n} must be multiplied with the zero-padding factor to fit the targets main lobe.

[1]Window optimized parameter for exponential parabolic interpolation p: Rectangular 0.777, Hanning 0.231, Nuttall 0.086.

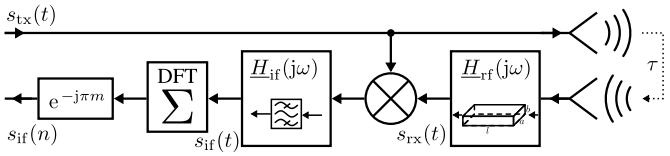

Fig. 6. Illustration of the influence of RF- and IF transfer function as well as the non-time-centered DFT dependent group delay on the IF signal.

According to Fig. 5 the FE algorithm can be described as follows:

1) Preprocessing of the sampled IF data $s_{\mathrm{if}}(n)$ by windowing, optional zero-padding and a DFT.
2) Coarse IF frequency evaluation by peak detection in $\underline{S}_{\mathrm{if}}(m)$ magnitude spectrum. Followed by a fine frequency estimation using interpolation and then distance calculation.

B. Phase Based Approach and Implementation Challenges

According to (3) it is possible that an estimation of phase

$$\hat{\varphi} = \arg\{\underline{S}_{\mathrm{if}}(\hat{m})\} \tag{11}$$

can be used to estimate the distance

$$\hat{R}_{\varphi} = \left[\pm\frac{\omega_0}{\dot{\omega}} \mp \sqrt{\left(\frac{\omega_0}{\dot{\omega}}\right)^2 - 2\frac{\hat{\varphi} \pm \phi_{\mathrm{r}}}{\dot{w}}}\right] \cdot \frac{c_{\mathrm{m}}}{2}, \quad 0 \le \pm\hat{\varphi} < \infty. \tag{12}$$

As the condition of the equation shows, the equation assumes an unambiguous estimated phase within $0 \le \pm\hat{\varphi} < \infty$. Hence, a simple evaluation of the phase information is only unambiguous within $-\pi \le \hat{\varphi} \le \pi$ and therefore insufficient for an unambiguous distance estimation in the entire measurement range. Since the native unambiguous range interval of PE is

$$R_{\varphi,\mathrm{un}} \approx \frac{2\pi}{\omega_0} \cdot \frac{c_{\mathrm{m}}}{2}. \tag{13}$$

Furthermore, with narrowband frequency ramps the expression $-\dot{\omega}^2/2$ in (3) is negligibly small and (12) can be simplified to

$$\hat{R}_{\varphi} \approx \frac{\pm\hat{\varphi} + \phi_{\mathrm{r}}}{\omega_0} \cdot \frac{c_{\mathrm{m}}}{2}. \tag{14}$$

An accurate PE requires that all phase responses in the radar systems radio frequency (RF) and IF paths are considered ($\underline{H}_{\mathrm{rf}}(\mathrm{j}\omega)$, $\underline{H}_{\mathrm{if}}(\mathrm{j}\omega)$ in Fig. 6). In this work, the major impact on the RF path phase response of the radar system is the propagation delay dispersion in the antenna feeding waveguide. The effect is more dramatic if the cutoff frequency of the waveguide ω_{wg} is close to the minimum radar chirp frequency $\omega_{\min}$. In the following, we take a closer look on the impact of rectangular waveguides in the radar systems RF path. The additional propagation delay due to the phase velocity $v_{\mathrm{p}}(t)$ (see [26]) in a single-mode used rectangular waveguide of length l_{wg} can be analytically described by

$$\begin{aligned}\tau_{\mathrm{d}}(t) &= \frac{2l_{\mathrm{wg}}}{v_{\mathrm{p}}(t)}, \quad -\frac{T_{\mathrm{R}}}{2} \le t \le \frac{T_{\mathrm{R}}}{2} \\ &= 2l_{\mathrm{wg}}\sqrt{1 - \left(\frac{\omega_{\mathrm{wg}}}{\omega_0 \pm \dot{\omega}t}\right)^2} \cdot \frac{1}{c_{\mathrm{m}}},\end{aligned} \tag{15}$$

where ω_{wg} is the waveguide cutoff frequency. By combining equations (3) and (15), the analytic IF signal disturbed by waveguide dispersion is given as

$$\begin{aligned}\underline{s}'^{+}_{\mathrm{if}}(t) &= \mathrm{e}^{\mathrm{j}\left[\dot{\omega}(\tau+\tau_{\mathrm{d}}(t))t \pm \omega_0(\tau+\tau_{\mathrm{d}}(t)) - \frac{1}{2}\dot{\omega}(\tau+\tau_{\mathrm{d}}(t))^2 \mp \phi_{\mathrm{r}}\right]} \\ &\approx \underbrace{\mathrm{e}^{\mathrm{j}\left[\dot{\omega}\tau t \pm \omega_0\tau - \frac{1}{2}\dot{\omega}\tau^2 \mp \phi_{\mathrm{r}}\right]}}_{=\underline{s}^{+}_{\mathrm{if}}(t)} \cdot \underbrace{\mathrm{e}^{\mathrm{j}[\dot{\omega}\tau_{\mathrm{d}}(t)t \pm \omega_0\tau_{\mathrm{d}}(t)]}}_{=\underline{w}_{\mathrm{rf}}(t)},\end{aligned} \tag{16}$$

where $\underline{w}_{\mathrm{rf}}(t)$ is a kind of continuous complex window function caused by waveguide dispersion. Hence, the spectrum is

$$\underline{S}'_{\mathrm{if}}(\mathrm{j}\omega) = \underline{S}_{\mathrm{if}}(\mathrm{j}\omega) * \underline{W}_{\mathrm{rf}}(\mathrm{j}\omega). \tag{17}$$

As demonstrated, the phase response in the RF path leads to a convolution of the ideal IF spectrum $\underline{S}_{\mathrm{if}}(\mathrm{j}\omega)$ with $\underline{W}_{\mathrm{rf}}(\mathrm{j}\omega) = \mathcal{F}\{\underline{w}_{\mathrm{rf}}(t)\}$. In consequence, $\underline{w}_{\mathrm{rf}}(t)$ causes pulse forming, a disturbing constant phase term and a frequency shift of the IF signal. Moreover, the spectral pulse of potentially disturbing radar targets is widened and thus leads to stronger spectral interferences with the main targets pulse.

In addition, the phase response in the IF path $\underline{H}_{\mathrm{if}}(\mathrm{j}\omega)$ should be considered:

$$\underline{S}''_{\mathrm{if}}(\mathrm{j}\omega) = \underline{S}'_{\mathrm{if}}(\mathrm{j}\omega) \cdot \underline{H}_{\mathrm{if}}(\mathrm{j}\omega). \tag{18}$$

The cause for an IF path transfer function is the IF filter structure. Particularly intermediate frequencies close to the cutoff frequency of high-order low or high pass filters cause large phase shifts. In contrast to the RF path phase response, $\underline{H}_{\mathrm{if}}(\mathrm{j}\omega)$ leads to an intermediate frequency dependent phase shift

$$\varphi''(\omega) = \varphi(\omega) + \varphi_{\mathrm{if}}(\omega), \quad \begin{matrix} 0 \le \pm\varphi(\omega) < \infty \\ 0 \le \varphi_{\mathrm{if}}(\omega) < \infty. \end{matrix} \tag{19}$$

Interesting and later useful is the fact that the sign of the ideal phase term compared to the IF path dependent phase shift $\varphi_{\mathrm{if}}(\omega)$ is reversed depending on the frequency chirp direction. Neglecting $\underline{H}_{\mathrm{if}}(\mathrm{j}\omega)$ would result in a distance dependent bias of

$$\hat{R}_{\varphi,\mathrm{e,if}}(R) = \pm\frac{\arg\left\{\underline{H}_{\mathrm{if}}\left(R\dot{\omega}\frac{2}{c_{\mathrm{m}}}\right)\right\}}{\omega_0}. \tag{20}$$

A second kind of IF path evoking phase shift is caused by the default non-time-centered DFT implementation

$$\mathrm{DFT}\{s_{\mathrm{if}}(n)\} = \sum_{n=0}^{N-1} s_{\mathrm{if}}(n) \cdot \mathrm{e}^{-\mathrm{j}\cdot 2\pi\frac{nm}{N}}. \tag{21}$$

Due to the frequency modulation dependent time base $-T_{\mathrm{R}}/2 \le t \le T_{\mathrm{R}}/2$ in (3) a kind of time-centered DFT

$$\begin{aligned}\underline{S}_{\mathrm{if}}(m) &= \sum_{n=0}^{N-1} s_{\mathrm{if}}(n) \cdot \mathrm{e}^{-\mathrm{j}\cdot 2\pi\frac{(n-\frac{N}{2})m}{N}} \\ &= \mathrm{DFT}\{s_{\mathrm{if}}(n)\} \cdot \mathrm{e}^{\mathrm{j}\pi m}\end{aligned} \tag{22}$$

must be used. This equation is valid if no zero-padding is applied. Using the non time-centered DFT would result in a frequency dependent phase shift

$$\varphi_{\mathrm{e,dft}}(\omega) = \arg\left\{\mathrm{e}^{-\mathrm{j}\frac{T_{\mathrm{R}}}{2}\omega}\right\} = -\frac{T_{\mathrm{R}}}{2}\omega \tag{23}$$

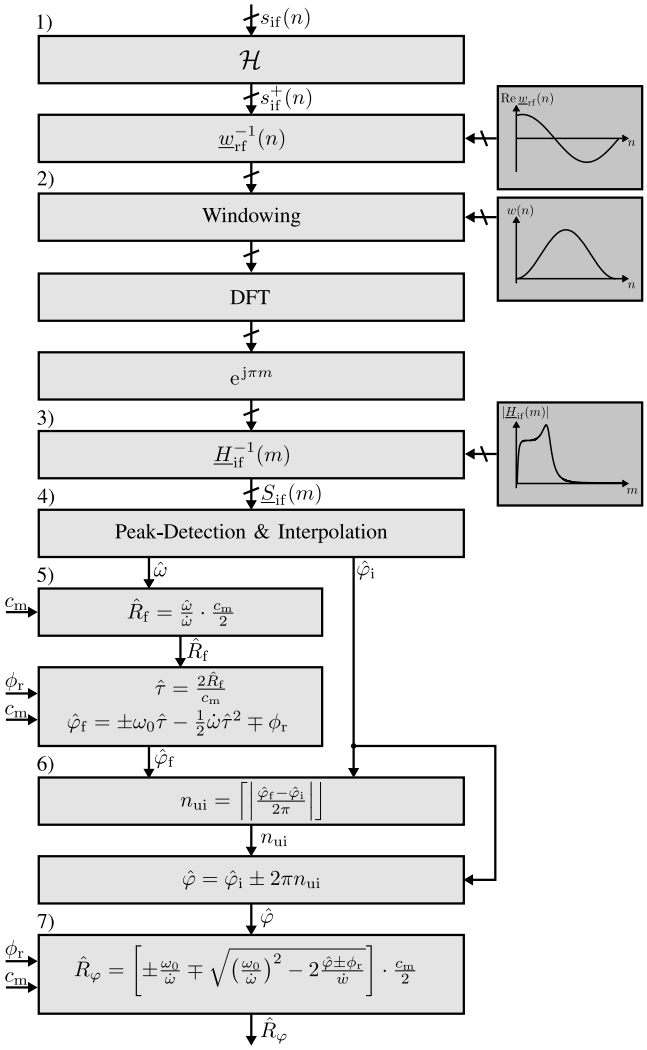

Fig. 7. Flow diagram of the basic phase evaluation algorithm.

in the continuous time domain and therefore in a distance dependent bias

$$\hat{R}_{\varphi,\mathrm{e,dft}}(R) \approx \mp\frac{T_{\mathrm{R}}\dot{\omega}}{2\omega_0}R. \tag{24}$$

III. Proposed Phase Evaluation Algorithm

A major problem of using the IF phase information for distance estimation is its limited unambiguity as shown in (13). Therefore, the idea of the proposed PE algorithm is the combination of the unambiguous FE with the ambiguous PE. Hardware and principle-based effects as described in Section II-B are considered.

A. Basic Phase Evaluation

According to Fig. 7 the basic PE algorithm is as follows:

1) Inverse filtering of the RF path transfer function by time domain division with the discrete complex window $\underline{w}_{\mathrm{rf}}(n)$, caused by the RF path transfer function. To avoid divisions by zero an analytical IF signal $\underline{s}_{\mathrm{if}}(n)$ and therefore a Hilbert transform of $s_{\mathrm{if}}(n)$ is required. For an analytical description of $\underline{w}_{\mathrm{rf}}(n)$ due to a propagation delay dispersion of a rectangular waveguide see (16). Alternatively, $\underline{w}_{\mathrm{rf}}(n)$ can be determined by measuring $\underline{s}_{\mathrm{if}}(n)$ and dividing by an idealized IF signal. This is useful when $\underline{w}_{\mathrm{rf}}(n)$ cannot be described analytically.
2) Windowing of the IF signal. As shown later in Section V, zero-padding is not essential. Computation of the time-centered DFT $\underline{S}_{\mathrm{if}}(m)$ by multiplication of the default DFT with $\exp(\mathrm{j}\pi m)$ as shown in (22). The IF Signal data vector can be left rotated by $N/2$ in time domain as an alternative to the complex multiplications.
3) Inverse filtering of the IF path related phase response by division with a precalculated simulation of $\underline{H}_{\mathrm{if}}(m)$.
4) Spectral peak-detection and interpolation of $\hat{m}_{\mathrm{i}}$ according to the FE methods described in Section II-A. The phase is estimated in the IF phase spectrum on previously estimated bin. As seen in Fig. 4, the curve of the phase spectrum near the target bin is widely flat. Thus, the phase at the interpolated frequency bin can be estimated by linear interpolation. However, this requires an introduction of a local phase unwrapping as described below to avoid false interpolation by phase jumps. First, interpolation is performed between the phase at the right bin

$$\hat{\varphi}_{\mathrm{ce}} = \hat{\varphi}(\lceil \hat{m}_{\mathrm{i}} \rceil) \tag{25}$$

and the possibly shifted phase at the left bin

$$\hat{\varphi}_{\mathrm{fl}} = \begin{cases} \hat{\varphi}(\lfloor \hat{m}_{\mathrm{i}} \rfloor) + 2\pi, & \text{for } \hat{\varphi}(\lceil \hat{m}_{\mathrm{i}} \rceil) - \hat{\varphi}(\lfloor \hat{m}_{\mathrm{i}} \rfloor) > \pi \\ \hat{\varphi}(\lfloor \hat{m}_{\mathrm{i}} \rfloor) - 2\pi, & \text{for } \hat{\varphi}(\lfloor \hat{m}_{\mathrm{i}} \rfloor) - \hat{\varphi}(\lceil \hat{m}_{\mathrm{i}} \rceil) > \pi \\ \hat{\varphi}(\lfloor \hat{m}_{\mathrm{i}} \rfloor), & \text{otherwise.} \end{cases} \tag{26}$$

Thus, the interpolated phase is

$$\hat{\varphi}_{\mathrm{i}}'(\hat{m}_{\mathrm{i}}) = \hat{\varphi}_{\mathrm{fl}} + [\hat{\varphi}_{\mathrm{ce}} - \hat{\varphi}_{\mathrm{fl}}](\hat{m}_{\mathrm{i}} - \lfloor \hat{m}_{\mathrm{i}} \rfloor). \tag{27}$$

Finally, the interpolated phase in target interval $[-\pi, \pi]$ is

$$\hat{\varphi}_{\mathrm{i}}(\hat{m}) = [\hat{\varphi}_{\mathrm{i}}'(\hat{m}_{\mathrm{i}}) + \pi] \bmod 2\pi - \pi. \tag{28}$$

5) Conversion of the intermediate frequency to a distance $\hat{R}_{\mathrm{f}}$ using the FE method. With (3), a virtual but absolute phase position of FE $\hat{\varphi}_{\mathrm{f}}$ is then calculated from $\hat{R}_{\mathrm{f}}$, where $\hat{\varphi}_{\mathrm{f}}$ is unambiguous over the entire measurement range.
6) The unambiguity phase interval

$$n_{\mathrm{ui}} = \arg\min_{n_{\mathrm{ui}}} |\hat{\varphi}(n_{\mathrm{ui}}, \hat{\varphi}_{\mathrm{i}}) - \hat{\varphi}_{\mathrm{f}}| = \left\lceil \left| \frac{\hat{\varphi}_{\mathrm{f}} - \hat{\varphi}_{\mathrm{i}}}{2\pi} \right| \right\rfloor \tag{29}$$

is then calculated by minimizing the difference between $\hat{\varphi}$ and $\hat{\varphi}_{\mathrm{f}}$, where $\lceil x \rfloor$ denotes the rounding to the nearest integer of x. The unambiguous phase over the entire measurement range is then determined by

$$\hat{\varphi} = \hat{\varphi}_{\mathrm{i}} \pm 2\pi n_{\mathrm{ui}}, \tag{30}$$

where $\hat{\varphi}_{\mathrm{i}}$ is the previously estimated ambiguous phase.
7) Based on $\hat{\varphi}$, an unambiguous and accurate estimation of the distance $\hat{R}_{\varphi}$ is performed with (12).

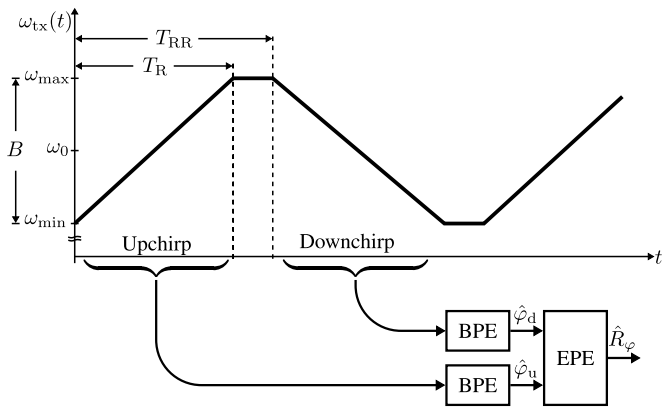

Fig. 8. Systematic overview of the working principle of the enhanced phase evaluation (EPE). A combination of two frequency ramps processed individually by basic phase evaluation (BPE).

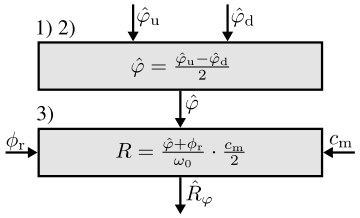

Fig. 9. Flow diagram of the enhanced phase evaluation algorithm, where $\hat{\varphi}_{\mathrm{u}}$ and $\hat{\varphi}_{\mathrm{d}}$ are determined according to the basic phase evaluation.

The virtual phase position of the FE $\hat{\varphi}_{\mathrm{f}}$ may have a maximum error of π. Thus, the maximum allowed distance error of the FE for a fully functional PE is

$$\hat{R}_{\mathrm{f,e}} \overset{!}{<} \frac{\pi}{\omega_0} \cdot \frac{c_{\mathrm{m}}}{2}, \tag{31}$$

when applied a non-distorted idealized PE.

B. Enhanced Phase Evaluation

The previously shown basic PE algorithm can be enhanced by combining up- and downchirps as shown in Fig. 8. In the following this is called enhanced PE. Absolute phases $\hat{\varphi}_{\mathrm{u}}$ and $\hat{\varphi}_{\mathrm{d}}$ are measured by the basic PE separately. According to (19) using means of $\hat{\varphi}_{\mathrm{u}}$ and $\hat{\varphi}_{\mathrm{d}}$ allows a full compensation of the phase response of the IF path. Therefore, any IF path depending bias on the estimated distance is eliminated. A coarse information about the IF path phase response is still required to determine the proper phase interval for the basic PE. The enhanced PE is especially suited when no accurate measurement of the IF frequency response is available, or it is affected by manufacturing tolerances. It is also suitable in cases where the IF path is influenced by thermal expansion or if there is a clock skew on the analog-to-digital converter that would cause a group delay, respectively. Considering Fig. 9, the enhanced PE works as follows:

1) Execution of a triangular-shaped frequency double ramp.
2) Separately applying of the basic PE.
3) Calculation of the means of the phase difference and subsequent estimation of the distance.

IV. Theoretical Comparison of the Performance

A. Precision Limits Given by the Cramér-Rao Bound

As a benchmark for the proposed algorithms the Cramér-Rao bound is used. The Cramér-Rao bound is the lower bound for the efficiency of an unbiased estimator. Therefore, it indicates the best estimation of the precision and thus the accuracy that can be achieved with the available biased data. The IF signal

$$s_{\mathrm{if,g}}(n) = A_{\mathrm{if}} \cdot \cos\left(2\pi \frac{\omega_{\mathrm{if}}}{\omega_{\mathrm{s}}} n\right) + g(n), \qquad 0 \le n < N \tag{32}$$

is assumed to be disturbed by additive white Gaussian noise $g(n)$. Therefore, the Cramér-Rao bound of the FE according to [8] is given as

$$\mathrm{Var}(\hat{R}_{\mathrm{f}}) \ge \frac{3c_{\mathrm{m}}^2}{\eta_{\mathrm{s/n}} N B^2}, \tag{33}$$

where $\eta_{\mathrm{s/n}}$ is the linear signal-to-noise ratio (SNR). Like the Cramér-Rao bound of FE there is a lower bound for the PE. According to [27] the Cramér-Rao bound for the estimated phase due to known frequency is

$$\mathrm{Var}(\hat{\varphi}) \ge \frac{1}{\eta_{\mathrm{s/n}} N}. \tag{34}$$

As a result, the Cramér-Rao bound for the PE is

$$\mathrm{Var}(\hat{R}_{\varphi}) \ge \frac{c_{\mathrm{m}}^2}{4\eta_{\mathrm{s/n}} N \omega_0^2}. \tag{35}$$

This equation requires an exactly estimated intermediate frequency beforehand.

B. Bias Caused by Disturbing Radar Targets

In the following, the distance bias induced by a single disturbing radar target using the FE $\hat{R}_{\mathrm{f,e,d}}$ and the PE $\hat{R}_{\varphi,\mathrm{e,d}}$ is analyzed. The main impact on the error when using FE is the relative amplitude between the main and the disturbing target. As well as the main lobe shape caused by the window function and the type of interpolation in IF magnitude spectrum. Therefore, the bias cannot be described analytically. Considering the range resolution (7) and constant main lobe width in bins following proportionality is derived:

$$\hat{R}_{\mathrm{f,e,d}} \propto \frac{1}{B}. \tag{36}$$

However, the relationship is different for PE than for FE. The resulting phase shift of a superposition of two harmonics with the same frequency but different amplitudes A_{a}, A_{b} and phases $\Delta\varphi$ is

$$\varphi_{\mathrm{a+b}} = \arctan\left(\frac{\sin(\Delta\varphi)}{\frac{A_{\mathrm{a}}}{A_{\mathrm{b}}} + \cos(\Delta\varphi)}\right). \tag{37}$$

Under consideration of (37) the maximum bias by a disturbing radar target using the PE is

$$\hat{R}_{\varphi,\mathrm{emax,d}} = \frac{\arctan\left(10^{\frac{A_{\mathrm{a,dB}} - A_{\mathrm{b,dB}}}{20}}\right)}{\omega_0} \cdot \frac{c_{\mathrm{m}}}{2} \propto \frac{1}{\omega_0}, \tag{38}$$

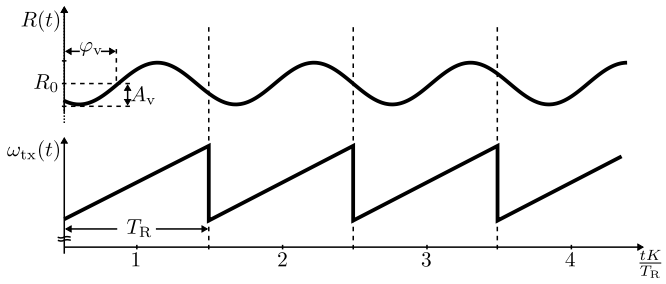

Fig. 10. Systematic representation of vibrating targets (top) during radar frequency chirps (bottom).

where $A_{\mathrm{a,dB}}$ is the amplitude of the main target and $A_{\mathrm{b,dB}}$ the amplitude of the disturbing target in dB. Considering a weak disturbing target, (38) can be simplified to

$$\hat{R}_{\varphi,\mathrm{emax,d}} \underset{A_{\mathrm{a,dB}} \gg A_{\mathrm{b,dB}}}{\approx} \frac{10^{\frac{A_{\mathrm{a,dB}}-A_{\mathrm{b,dB}}}{20}}}{\omega_0} \cdot \frac{c_\mathrm{m}}{2}. \tag{39}$$

Hence, the mentioned bias of the PE does not depend on the radar bandwidth B but on the center frequency ω_0 when compared with the FE.

C. Reduction of Precision by the Micro-Doppler Effect

In a lot of real field applications, the distance to be measured is not static but disturbed by micro vibrations. Therefore, the estimated distance is not constant (see Fig. 10). It oscillates with an angular frequency ω_v and an amplitude A_v in a distance R_0:

$$R(t) = R_0 + A_\mathrm{v} \sin[\omega_\mathrm{v}(t + kT_\mathrm{r}) + \varphi_\mathrm{v}], \qquad k \in \mathbb{Z}, \tag{40}$$

where φ_v is the zero-phase angle of the disturbing oscillation and k is the index of the related radar frequency chirp. For simplicity, it is assumed that the ramp repetition time T_RR is equal to the ramp duration T_R. Using (3) and a Taylor series approach the estimated frequency is

$$\begin{aligned}\hat{\omega}_\mathrm{v} =& \dot{\omega}\frac{2}{c_\mathrm{m}} R_0 + \dot{\omega}\frac{2}{c_\mathrm{m}} A_\mathrm{v} \sin(\omega_\mathrm{v} k T_\mathrm{R} + \varphi_\mathrm{v}) \\ &\pm \omega_0 \frac{2}{c_\mathrm{m}} A_\mathrm{v} \omega_\mathrm{v} \cos(\omega_\mathrm{v} k T_\mathrm{R} + \varphi_\mathrm{v}).\end{aligned} \tag{41}$$

The equation consists of three terms. These terms belong to the mean distance R_0, the distance modulation and the distance modulation depending on the Doppler effect. Considering the estimated frequency from ramp k to $k+1$ then $\hat{\omega}_\mathrm{v}$ is a superposition by two 90-degree phase shifted harmonics with frequency T_R. Consequently, the impact on random errors using the FE is

$$\mathrm{Var}(\hat{R}_{\mathrm{f,v}}) = \frac{A_\mathrm{v}^2}{2\dot{\omega}^2}\left(\dot{\omega}^2 + w_0^2 \omega_\mathrm{v}^2\right) + \mathrm{Var}(\hat{R}_\mathrm{f}). \tag{42}$$

With the same approach used in (41) the estimated IF phase of a vibrating radar target is

$$\hat{\varphi}_\mathrm{v} = \omega_0 \frac{2}{c_\mathrm{m}} R_0 + \omega_0 \frac{2}{c_\mathrm{m}} A_\mathrm{v} \sin(\omega_\mathrm{v} k T_\mathrm{R} + \varphi_\mathrm{v}). \tag{43}$$

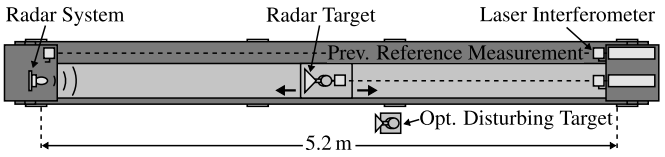

Fig. 11. Top-down schematic of the experimental setup. The upper illustration of a laser interferometer belongs to a previous reference measurement for compensating of the linear track warping caused by the moving carriage. The optional disturbing target is part of the measurements performed in Section IV-B.

TABLE II
RADAR SENSOR SPECIFICATIONS

Parameter	Value
Center Frequency	80 GHz
Bandwidth	24 GHz
Operation Mode	Linear Modulation[a]
Chirp Time	2048 µs
Chirp Rate	488 Hz / 244 Hz[b]
Sampling Rate	1 MS/s
TX Power	−6 dBm[c]
In-loop Phase Noise	−85 dBc/Hz[d]
Antenna	28 dBi dielectric lens [28]

[a] Dual-Loop PLL synthesizer
[b] Single ramps / alternating ramps
[c] At antenna
[d] At 1 kHz to 1 MHz offset

In comparison to the FE, only two terms can be observed. A harmonic by the Doppler shift is not present. Analogously the variance using the PE is

$$\mathrm{Var}(\hat{R}_{\varphi,\mathrm{v}}) = \frac{A_\mathrm{v}^2}{2} + \mathrm{Var}(\hat{R}_\varphi). \tag{44}$$

To compare the FE with the PE according to their effect on random errors due to vibrating radar targets it is useful to examine the relationship

$$\frac{\mathrm{Var}(\hat{R}_{\mathrm{f,v}})}{\mathrm{Var}(\hat{R}_{\varphi,\mathrm{v}})} \underset{\eta_{\mathrm{s/n}} \gg 1}{\approx} \frac{\dot{\omega}^2 + \omega_0^2 \omega_\mathrm{v}^2}{\dot{\omega}^2} \geq 1 \tag{45}$$

between (42) and (44). The quotient is always greater or equal to one. For this reason, the measurement stability of vibrating targets with PE is always better than with FE. Typically, a type of triangular-shaped frequency modulation that is not considered here is used to eliminate the Doppler effect in FE. But with vibration frequencies ω_v that are in region of the ramp duration T_R this does not work. An interesting side effect of this relation is that it can be used for target identification in multi target environments.

V. SIMULATION AND MEASUREMENT RESULTS

A. Experimental Setup

We performed several measurements with an 80 GHz wideband radar platform introduced in [2], [3]. Table II shows the radar sensor specifications and configurations. To carry out isolated investigations of specific effects, simulations with the

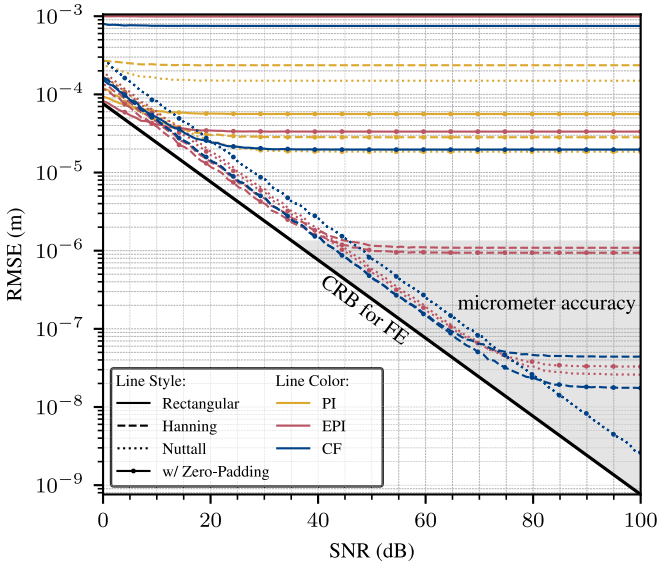

Fig. 12. Simulated root-mean-square error (RMSE) by frequency evaluation (FE) for parabolic interpolation (PI), exponential parabolic interpolation (EPI) and center formula (CF) by random repositioning the target for each data point to illustrate the effect of spectral leakage. Different window functions (rectangular, Hanning, Nuttall) and optional two times zero-padding were used. The simulated target was randomly moved over the entire measurement range. The Cramér-Rao bound serves as a lower bound of the RMSE. Some lines with and without zero-padding are overlapped.

same configuration used for measurements were performed. As radar targets we utilized corner reflectors with 5, 7 and 14 cm edge length. The respective target was situated on a tilted bar on the linear track with a maximum working range of 5.2 m and a positioning repeatability of 10 µm (see Fig. 11). The entire measurement setup was built on top of a solid granite slab to reduce the influence of the environment. Furthermore, the radar system used to evaluate the proposed algorithm and a laser interferometer were installed on two opposite sides measuring the distance to the moving target. The environmentally compensated laser interferometer HPI-3D from Lasertex served as a reference distance measurement instrument providing an accuracy of 0.4 µm per measured distance meter according to its specification. In order to compensate the influence of bending granite slabs caused by the moving mass of the carriage, a reference measurement between radar and laser interferometer was performed beforehand. To reduce possible sources of inaccuracy, the FMCW radar systems reference clock was augmented by an ovenized quartz oscillator, thus providing a much more temperature stable reference for target distance measurements. In contrast to [1] we modified the radar backend using a system on chip with programmable logic. It provides a system trigger structure that is synchronous to the phase-locked loop clock, resulting in a more precise distance estimation.

B. Verification and Comparison of the Methods

Fig. 12 shows several FE simulation results with different evaluation configurations. For each data point the simulated point target was randomly positioned along the range axis in an idealized environment. In addition, the IF signals were disturbed by additive white Gaussian noise to achieve a certain SNR. Then, for each configuration, the root-mean-square error (RMSE) of the simulated distance error was calculated to show which configuration is suitable for micrometer distance measurements caused by the picket-fence effect (see [29]) due to spectral leakage. Three different kinds of window functions with a highly varying main lobe width and side-lobe suppression were used (see [29], [30]).[2] Nuttall window refers to the four term Nuttall window with continuous first derivative. As can be seen, at a high SNR the RMSE is dominated by a bias due to spectral leakage regardless of the configuration used. Only a few combinations are suitable for micrometer accurate distance measurement. Especially the exponential parabolic interpolation or the center formula with Hanning or Nuttall windows are applicable (as marked). In addition, Fig. 12 shows that zero-padding is not essential and can therefore be omitted due to the increase in computational load by the DFT with the increasing number of data samples.[3]

To compare FE with PE according the limits given by the Cramér-Rao bounds, we performed precision measurements with a 5 cm corner reflector. In Fig. 13 the measured and simulated standard deviation of the FE is compared with the PE using 1000 measurements at each point. The distance deviation of the PE is superior to that of the FE over the entire range. As a result, the measured stability of PE at 0.4 m is less than 50 nm and therefore it is close to the limits caused by mechanical environmental oscillations. In 5.6 m the stability is still less than 600 nm compared to FE with more than 10 µm.

Fig. 14 shows several simulations and measurements of the bias caused by disturbing radar targets. The parameters of comparison are the relative power and distance. FE is compared with PE as well as the exponential parabolic interpolation with the center formula. For the measurements, a static interfering target was positioned beside the linear track (see Fig. 11). As can be seen, each measurement and simulation is overlaid by an oscillation. This is due to the fact that the radar target interferes alternately constructively and destructively with the disturbing radar target in the IF signal, depending on its distance-periodic phase. The main insight of this figure is the significantly larger bias at distance differences above 15 mm by using the center formula compared to the exponential parabolic interpolation. The reason for this is that ten rather than three bins are used for calculation. Therefore, the exponential parabolic interpolation compared with center formula is the better choice for the FE according real and thus disturbed radar environments. Since real targets are extended and non-point-shaped, they also lead to interferences in the IF signal due to path differences of the backscattered multiple reflections. The wave approaching the extended target cannot be considered plane, especially at short distances. As can be seen particularly in Fig. 14(b), these interferences lead

[2]-3 dB main-lobe bandwidth / Highest side-lobe level (Bins / dB): Rectangular: 0.89 / -13, Hanning: 1.44 / -18, Nuttall: 1.91 / -93.

[3]Computational load of the Cooley-Tukey fast Fourier transform (FFT) algorithm: $\mathcal{O}(N \log_2 N)$.

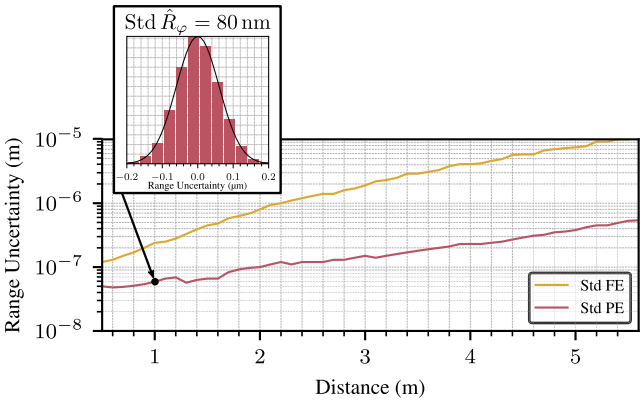

(a) Measured distance uncertainty using a 5 cm corner reflector.

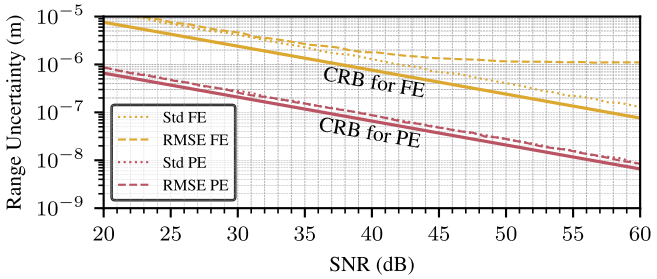

(b) Simulated distance uncertainty. Comparison with Cramér-Rao bounds.

Fig. 13. Measured and simulated distance uncertainty of frequency evaluation (FE) and phase evaluation (PE). The measured PE result is close to the limit by unwanted mechanical vibrations. The significant improvement of the measured PE precision compared to the previous work [1] is caused by the improved system trigger structure.

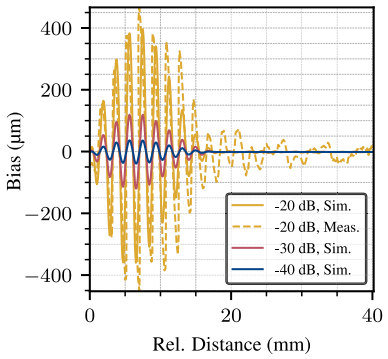

(a) Frequency evaluation using the exponential parabolic interpolation.

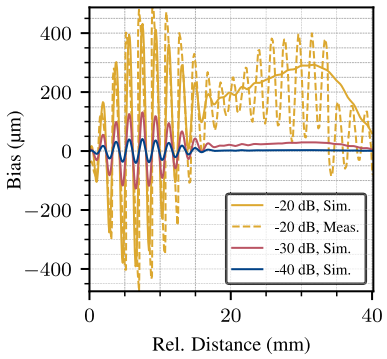

(b) Frequency evaluation using the center formula.

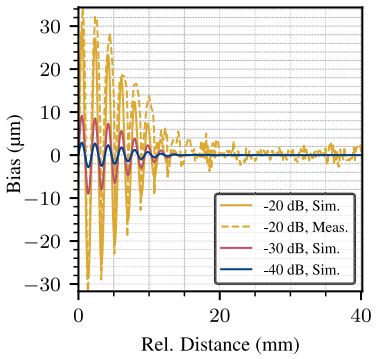

(c) Phase Evaluation using the exponential parabolic interpolation.

Fig. 14. Simulated and measured distance bias caused by disturbing targets depending on relative target distance- and power. Comparison of the frequency evaluation and the phase evaluation with different interpolation methods. A Hanning window was used.

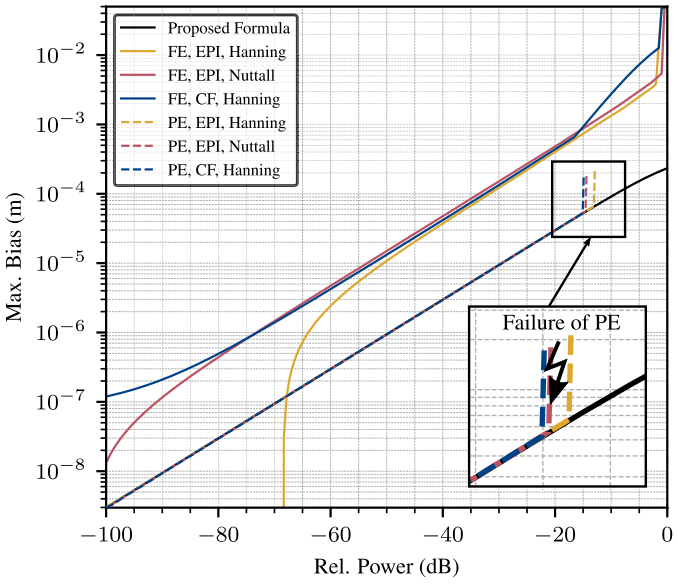

Fig. 15. Simulated maximum distance bias due to disturbing targets. Comparison of different frequency interpolation methods (exponential parabolic interpolation and center formula, labeled as EPI and CF), window functions (Hanning, Nuttall) with frequency evaluation (FE), phase evaluation (PE) and the proposed formula (38). Representation of the failure of PE by a strong disturbing target due to violation of (31).

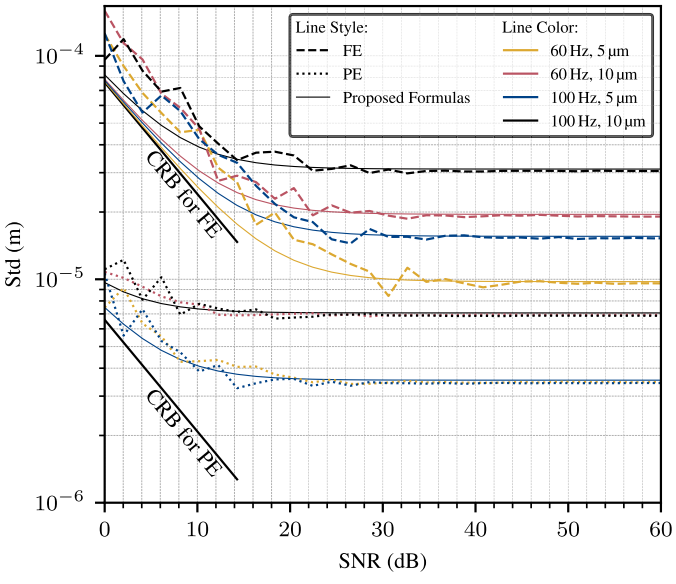

Fig. 16. Simulated standard deviation of micro-Doppler disturbed distance measurements for frequency evaluation (FE) and phase evaluation (PE) with mentioned vibration frequencies (60, 100 Hz) and amplitudes (5, 10 µm). Comparison with the proposed formulas (42), (44) and the Cramér-Rao bounds as the lower bounds for standard deviation of static radar targets.

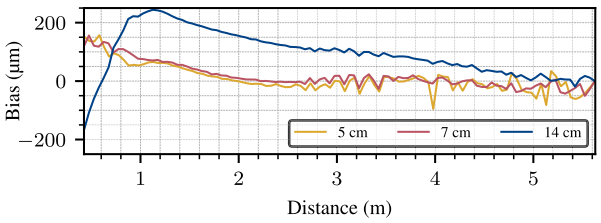

(a) Frequency Evaluation

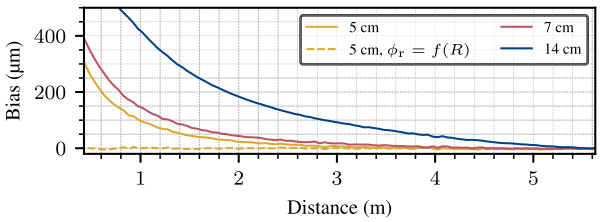

(b) Enhanced Phase Evaluation

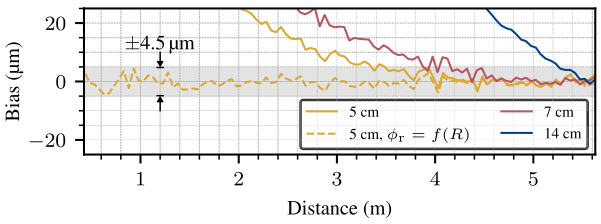

(c) Enhanced Phase Evaluation (Detailed View)

Fig. 17. Measured distance bias by using corner reflectors of different sizes (5, 7, 14 cm). Comparison of the frequency evaluation with the enhanced phase evaluation using a constant target reflection phase ϕ_r as well as a distance dependent ϕ_r for a 5 cm corner reflector.

to a superposition of additional oscillations on the measured distances compared to the simulations. Fig. 15 shows essentially the same simulations as in Fig. 14 but from a different view. FE is compared with PE as well as the various evaluation configurations by showing the maximum bias to be expected with the relative power of the radar targets. Equation (38) was confirmed as well as the superiority of PE over FE. The bias on PE especially by disturbers with high radar cross section is about ten times smaller than FE. Thus, the exponential parabolic interpolation with Hanning window should be used to estimate proper PE results over a wide range.

Fig. 16 shows standard deviations of several micro-Doppler shifted simulations to confirm the proposed formulas (42) and (44). Different kinds of oscillations were modulated on R_0. FE, PE, as well as the Cramér-Rao bounds are plotted. As the figure shows, (42) and (44) were proven. When using the FE, the standard deviation is dominated by the oscillation and the micro-Doppler effect at high SNR. But with PE, the simulation is only affected by the oscillation itself. In addition, (45) was confirmed by a 100 Hz disturbed measurement caused by an enabled position control of the linear track. The measured value for $\mathrm{Var}(\hat{R}_{\mathrm{f,v}})/\mathrm{Var}(\hat{R}_{\varphi,\mathrm{v}})$ of a radar target at 1.5 m was 19.2 and therefore close to the theoretical expected value of 19.4.

C. Achieved Measurement Accuracy

We performed multiple measurements to estimate the accuracy of the proposed PE algorithm with the used radar system.

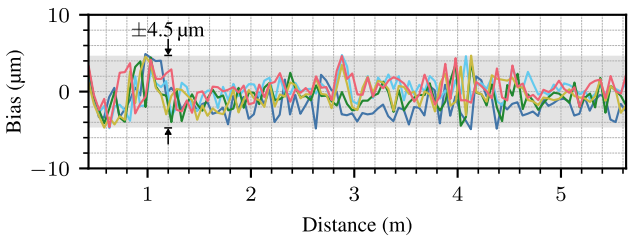

Fig. 18. Bias of five independent distance measurements with enhanced phase evaluation to demonstrate the measurement repeatability. Using the same calibration measurement for the target reflection phase ϕ_r. A corner reflector with 5 cm edge length was utilized.

Additionally, we compared the results with the FE methods. A Hanning window with exponential parabolic interpolation was used. Fig. 17 shows the measurement results of FE and PE by using corner reflectors of different sizes. It can be recognized a large bias on the FE that is caused by disturbing targets. Thus, the measured distance bias of FE is about ±120 µm. The PE, on the other hand, is affected to a much lesser extent as shown in Section IV-B theoretically. The distance bias of the PE is less than ±4.5 µm in the range of 3.5 to 5.6 m by using a small 5 cm corner reflector. Furthermore, the increasing bias of the PE at short distances is systematic and reproducible for the respective types and sizes of radar targets. This behavior can be described by a distance dependent target reflection phase ϕ_r (see (3)) due to backscattered multiple reflections of an extended and non-point-shaped target as described in Section V-B. Therefore, ϕ_r is the variation of the phase center of the radar target with respect to the distance. To consider the distance dependent target reflection phase, we performed a dedicated calibration measurement series with the reference system. Using the measured distance error of PE, we estimated ϕ_r as a function of R with an 8th order polynomial fit. As can be seen in Fig. 17(c), PE is accurate over the entire measurement range of 5.2 m within ±4.5 µm. To demonstrate the repeatability of the accuracy measurements, we reproduced it five independent times using the same calibration for ϕ_r, as shown in Fig. 18.

VI. Conclusion

We have shown that the used 80 GHz FMCW radar system highly benefits from the proposed phase evaluation algorithm compared to the classic frequency evaluation approach. Accuracies of ±4.5 µm were achieved over the entire measurement range of at least 5.2 m using a laser interferometer as a reference. To the best of the authors' knowledge the achieved distance accuracy over the large range variation is a record value and is also close to measurement limits caused by thermal expansion of the experimental setup, mechanical alignment issues or limits of the reference laser interferometer system. In addition, the measured repeatability by the proposed phase evaluation is within standard deviation of about 80 nm · m^{-1}. It was experimentally confirmed that the standard deviation of the proposed algorithm is 17 times smaller than that of the frequency evaluation. Furthermore, we have investigated the bias induced by disturbing radar targets through a derivation of the theoretical boundaries and several simulations as well as

measurements. The maximum distance error of the phase evaluation compared with the frequency evaluation was minimized by at least ten times. Additionally, the increase of distance uncertainty by the micro-Doppler effect due to vibrations was analyzed. We have derived the theoretical limits and proved them by simulations. For example, the standard deviation of a distance estimation by a radar target that oscillates with 200 Hz was reduced approximately by a factor of 8.5 independent of the oscillation amplitude.

To achieve the above specifications, a novel phase evaluation algorithm was designed. This algorithm works without a history or a sophisticated filter structure and it enables the highest accuracy with low vulnerability to interferences. In addition, costly arithmetic operations are avoided. Thus, it allows for implementation on low-cost, low-performance and energy-efficient computing systems.

Considering their high robustness and cost-effectiveness, phase evaluating FMCW radar systems can be used as alternatives to expensive optical systems by utilizing the proposed algorithm as presented here.

ACKNOWLEDGMENT

The authors would like to thank Infineon Technologies AG for fabricating the radar chips. They would also like to thank Status Pro Maschinenmesstechnik GmbH for aligning the straightness of the measurement setup.

REFERENCES

[1] L. Piotrowsky, T. Jaeschke, S. Kueppers, and N. Pohl, "An unambiguous phase-based algorithm for single-digit micron accuracy distance measurements using FMCW radar," in *IEEE MTT-S Int. Microw. Symp. Dig.*, Jun. 2019, pp. 552–555.

[2] N. Pohl, T. Jaeschke, and K. Aufinger, "An ultra-wideband 80 GHz FMCW radar system using a SiGe bipolar transceiver chip stabilized by a fractional-N PLL synthesizer," *IEEE Trans. Microw. Theory Techn.*, vol. 60, no. 3, pp. 757–765, Mar. 2012.

[3] N. Pohl, T. Jaeschke, S. Kueppers, C. Bredendiek, and D. Nüßler, "A compact ultra-wideband mmWave radar sensor at 80 GHz based on a SiGe transceiver chip (focused session on highly-integrated millimeter-wave radar sensors in SiGe BiCMOS technologies)," in *Proc. Int. Microw. Radar Conf. (MIKON)*, May 2018, pp. 345–347.

[4] Q. Guoqing, "High accuracy range estimation of FMCW level radar based on the phase of the zero-padded FFT," in *Proc. Int. Conf. Signal Process.*, Aug./Sep. 2004, pp. 2078–2081.

[5] S. Rahman, P. V. Brennan, and L. Lok, "Millimeter-precision range profiling and cross-sectional imaging of ice shelves in polar regions using phase-sensitive FMCW radar," in *Proc. IEEE Radar Conf. (RadarCon)*, Apr./May 2013, pp. 1–5.

[6] S. Ayhan, S. Scherr, P. Pahl, T. Kayser, M. Pauli, and T. Zwick, "High-accuracy range detection radar sensor for hydraulic cylinders," *IEEE Sensors J.*, vol. 14, no. 3, pp. 734–746, Mar. 2014.

[7] P. V. Brennan, K. Nicholls, L. B. Lok, and H. Corr, "Phase-sensitive FMCW radar system for high-precision Antarctic ice shelf profile monitoring," *IET Radar, Sonar Navigat.*, vol. 8, no. 7, pp. 776–786, Aug. 2014.

[8] S. Scherr, S. Ayhan, B. Fischbach, A. Bhutani, M. Pauli, and T. Zwick, "An efficient frequency and phase estimation algorithm with CRB performance for FMCW radar applications," *IEEE Trans. Instrum. Meas.*, vol. 64, no. 7, pp. 1868–1875, Jul. 2015.

[9] M. Pauli *et al.*, "Miniaturized millimeter-wave radar sensor for high-accuracy applications," *IEEE Trans. Microw. Theory Techn.*, vol. 65, no. 5, pp. 1707–1715, May 2017.

[10] M. Z. Ikram, A. Ahmad, and D. Wang, "High-accuracy distance measurement using millimeter-wave radar," in *Proc. IEEE Radar Conf. (RadarConf)*, Apr. 2018, pp. 1296–1300.

[11] T. Musch, "A high precision 24-GHz FMCW radar based on a fractional-N ramp-PLL," *IEEE Trans. Instrum. Meas.*, vol. 52, no. 2, pp. 324–327, Apr. 2003.

[12] N. Pohl, M. Gerding, B. Will, T. Musch, J. Hausner, and B. Schiek, "High precision radar distance measurements in overmoded circular waveguides," *IEEE Trans. Microw. Theory Techn.*, vol. 55, no. 6, pp. 1374–1381, Jun. 2007.

[13] C. Bredendiek, N. Pohl, T. Jaeschke, S. Thomas, K. Aufinger, and A. Bilgic, "A 24 GHz wideband single-channel SiGe bipolar transceiver chip for monostatic FMCW radar systems," in *Proc. Eur. Microw. Integr. Circuit Conf.*, Oct. 2012, pp. 309–312.

[14] T. Jaeschke, M. Vogt, C. Baer, C. Bredendiek, and N. Pohl, "Improvements in distance measurement and SAR-imaging applications by using ultra-high resolution mm-wave FMCW radar systems," in *IEEE MTT-S Int. Microw. Symp. Dig.*, Jun. 2012, pp. 1–3.

[15] N. Pohl *et al.*, "Radar measurements with micrometer accuracy and nanometer stability using an ultra-wideband 80 GHz radar system," in *Proc. IEEE Top. Conf. Wireless Sensors Sensor Netw. (WiSNet)*, Jan. 2013, pp. 31–33.

[16] M. G. Girma *et al.*, "Miniaturized 122 GHz system-in-package (SiP) short range radar sensor," in *Proc. Eur. Radar Conf.*, Oct. 2013, pp. 49–52.

[17] S. Lindner, F. Barbon, S. Mann, G. Vinci, R. Weigel, and A. Koelpin, "Dual tone approach for unambiguous six-port based interferometric distance measurements," in *IEEE MTT-S Int. Microw. Symp. Dig.*, Jun. 2013, pp. 1–4.

[18] G. Vinci *et al.*, "A six-port radar system for precise distance measurements and vibration monitoring in industrial environments," in *Proc. Sensors Measuring Syst.*, Jun. 2014, pp. 1–5.

[19] T. Jaeschke, C. Bredendiek, S. Kueppers, and N. Pohl, "High-precision D-band FMCW-radar sensor based on a wideband SiGe-transceiver MMIC," *IEEE Trans. Microw. Theory Techn.*, vol. 62, no. 12, pp. 3582–3597, Dec. 2014.

[20] S. Scherr, S. Ayhan, H. Gulan, M. Pauli, and T. Zwick, "61 GHz ISM band FMCW radar for applications requiring high accuracy," in *Proc. Asia–Pacific Microw. Conf.*, Nov. 2014, pp. 1118–1120.

[21] S. Scherr *et al.*, "Miniaturized 122 GHz ISM band FMCW radar with micrometer accuracy," in *Proc. Eur. Radar Conf. (EuRAD)*, Sep. 2015, pp. 277–280.

[22] S. Scherr *et al.*, "Influence of radar targets on the accuracy of FMCW radar distance measurements," *IEEE Trans. Microw. Theory Techn.*, vol. 65, no. 10, pp. 3640–3647, Oct. 2017.

[23] F. Herzel, D. Kissinger, and H. J. Ng, "Analysis of ranging precision in an FMCW radar measurement using a phase-locked loop," *IEEE Trans. Circuits Syst., I, Reg. Papers*, vol. 65, no. 2, pp. 783–792, Feb. 2018.

[24] G. S. Woods, D. L. Maskell, and M. V. Mahoney, "A high accuracy microwave ranging system for industrial applications," *IEEE Trans. Instrum. Meas.*, vol. 42, no. 4, pp. 812–816, Aug. 1993.

[25] M. Gasior, "Improving frequency resolution of discrete spectra," Ph.D. dissertation, Dept. Elect. Eng., AGH Univ. Sci. Technol., Kraków, Poland, 2006.

[26] N. J. Cronin, *Microwave and Optical Waveguides*. London, U.K.: Institute of Physics, 1995.

[27] S. M. Kay, *Fundamentals of Statistical Signal Processing: Estimation Theory*, vol. 1. Upper Saddle River, NJ, USA: Prentice-Hall, 1993.

[28] N. Pohl and M. Gerding, "A dielectric lens-based antenna concept for high-precision industrial radar measurements at 24 GHz," in *Proc. Eur. Microw. Conf.*, Oct./Nov. 2012, pp. 731–734.

[29] F. J. Harris, "On the use of windows for harmonic analysis with the discrete Fourier transform," *Proc. IEEE*, vol. 66, no. 1, pp. 51–83, Jan. 1978.

[30] A. H. Nuttall, "Some windows with very good sidelobe behavior," *IEEE Trans. Acoust., Speech, Signal Process.*, vol. ASSP-29, no. 1, pp. 84–91, Feb. 1981.

Lukas Piotrowsky (S'18) was born in Neuwied, Germany, in 1990. He received the B.Sc. degree from the Koblenz University of Applied Sciences, Koblenz, Germany, in 2016, and the M.Sc. degree in electrical and information engineering from Ruhr University Bochum, Bochum, Germany, in 2018.

Since 2018, he has been a Research Assistant with the Institute of Integrated Systems, Ruhr University Bochum. His current research interests include millimeter-wave radar system design and embedded signal processing.

Timo Jaeschke (S'07–M'17) was born in Hattingen, Germany, in 1984. He received the Dipl.-Ing. and Dr.-Ing. degrees in electrical engineering from Ruhr University Bochum, Bochum, Germany, in 2011 and 2017, respectively.

From 2011 to 2018, he was a Research Assistant with the Institute of Integrated Systems, Ruhr University Bochum. He currently is the CEO of the newly founded 2π-Labs GmbH, Bochum, a precision mmW-Sensor company. His current research interests include frequency synthesis, integrated ultra-wideband frequency-modulated continuous-wave (FMCW) radar systems up to 240 GHz, high-resolution radar imaging, and highest precision distance and vibration measurements for various applications.

Dr. Jaeschke is a member of the VDE, ITG, EuMA, and DGON. He was the recipient of the IEEE Microwave Theory and Techniques Society (IEEE MTT-S) Graduate Fellowship Award in 2013 and the Airbus Defence and Space ARGUS Award in 2010. He was a co-recipient of the EuMIC Prize in 2012.

Simon Kueppers (S'17) was born in Oberhausen, Germany, in 1988. He received the M.Sc. degree in electrical engineering from Ruhr University Bochum, Bochum, Germany, in 2014, where he is currently pursuing the Ph.D. degree in system architectures for MIMO radar systems.

In 2015, he joined the Fraunhofer Institute for High-Frequency Physics and Radar Techniques FHR, Wachtberg, Germany, where he was involved in the research on system architectures for millimeter-wave MIMO radar systems. He is currently a Chief Technology Officer with 2π-Labs GmbH, Bochum.

Jan Siska (S'18) received the B.Sc. and M.Sc. degrees in electrical and information engineering from Ruhr University Bochum, Bochum, Germany, in 2015 and 2018, respectively, where he is currently pursuing the Ph.D. degree at the Institute of Integrated Systems.

His current research interests include high-resolution SAR imaging and vital sign detection using FMCW radar sensors.

Nils Pohl (GS'07–M'11–SM'14) received the Dipl.-Ing. and Dr.-Ing. degrees in electrical engineering from Ruhr University Bochum, Bochum, Germany, in 2005 and 2010, respectively.

From 2006 to 2011, he was a Research Assistant with Ruhr University Bochum, where he was involved in integrated circuits for millimeter-wave (mm-wave) radar applications. In 2011, he became an Assistant Professor with Ruhr University Bochum. In 2013, he was the Head of the Department of mm-Wave Radar and High-Frequency Sensors, Fraunhofer Institute for High Frequency Physics and Radar Techniques, Wachtberg, Germany. In 2016, he was a Full Professor for integrated systems with Ruhr University Bochum. He has authored or coauthored more than 100 scientific articles and has issued several patents. His current research interests include ultra-wideband mm-wave radar, design, and optimization of mm-wave integrated SiGe circuits and system concepts with frequencies up to 300 GHz and above, as well as frequency synthesis and antennas.

Dr. Pohl is a member of the VDE, ITG, EUMA, and URSI. He was a co-recipient of the 2009 EEEfCom Innovation Award, the 2012 EuMIC Prize, and the 2015 Best Demo Award of IEEE Radio Wireless Week and a recipient of the Karl-Arnold Award of the North Rhine-Westphalian Academy of Sciences, Humanities and the Arts in 2013 and the IEEE MTT-S Outstanding Young Engineer Award in 2018.